Analysis and Dynamic Control of a Dual-Stator BDFIG-DC System Supplying DC Grid With Minimized Torque Ripple Through Harmonic Current Injection

Yunlei Jiang, *Student Member, IEEE*, Ming Cheng, *Fellow, IEEE*, Peng Han, *Member, IEEE*, Qingsong Wang, *Senior Member, IEEE*, and Xiaohu Wang

***Abstract*—Due to inherent high reliability and low maintenance cost, the brushless doubly fed induction generator (BDFIG) has become a promising candidate in offshore wind energy generation systems and dc/ac/hybrid microgrids. This paper proposes a novel BDFIG based system targeting at dc power generation (BDFIG-DC), which features interfacing the power winding (PW) and the dc grid through an uncontrolled rectifier and common dc link. Compared to conventional BDFIG systems fed by ac grid, the BDFIG-DC system offers an alternative to integrate the BDFIG into the dc transmission system with a simpler structure and lower cost. Due to the constraint imposed by the dc-side diode bridge, torque ripple reduction emerges as an urgent issue as a result of the distorted flux and current. To achieve the smooth dc-connected operation of the BDFIG, an improved vector control strategy is proposed in this paper, where the control of the system is divided into three parts: torque ripple reduction, frequency regulation, and average torque control. Based on the investigations into the electromagnetic torque reduction and small-signal model of the PW flux linkage, average torque and PW frequency are successfully controlled with torque ripple effectively suppressed. The effectiveness of the proposed system, along with the associated control strategy, is validated by the experimental results of a 10-kW 2/1 dual-stator BDFIG (DS-BDFIG) prototype.**

***Index Terms*—Brushless doubly fed induction generator (BDFIG), dc grid, dual stator, torque ripple reduction.**

Manuscript received January 23, 2018; revised June 27, 2018; accepted August 14, 2018. Date of publication August 27, 2018; date of current version April 20, 2019. This work was supported by the National Natural Science Foundation of China under Project 51320105002. Recommended for publication by Associate Editor D. Dujic. *(Corresponding author: Ming Cheng.)*

Y. Jiang was with the School of Electrical Engineering, Southeast University, Nanjing 210096, China. He is now with the Department of Electrical and Computer Engineering, Wisconsin Electric Machines and Power Electronics Consortium (WEMPEC), University of Wisconsin-Madison, Madison, WI 53706 USA (e-mail:

Then, alternative solutions have been proposed recently to interface the doubly fed induction generator (DFIG) with the dc grid [4]–[10], from fundamental operation issues, decoupled torque, and frequency regulation to torque ripple reduction. In the conventional ac-grid-connected system, the stator is directly connected to the ac grid while the rotor is fed by a set of back-to-back converters. In [4], a DFIG-DC system is initially introduced and modeled, in which the grid-side converter (GSC) is replaced by a diode bridge and both the diode bridge and the rotor-side converter (RSC) are connected to the same dc grid. In [5], the stator frequency was mainly focused on and the small-signal model appropriate for the frequency control was derived. In [6], speed sensorless operation of the DFIG-DC system is realized by applying a modified phase-locked loop on the stator voltage. Considering inherent harmonics imposed by the diode bridge, suppression of electromagnetic torque ripple is then taken into consideration in [7] with the help of an added resonant current controller. Furthermore, a direct resonant strategy is developed in [8] to suppress the torque ripple based on an investigation into torque ripple mechanism of the DFIG-DC system. In [9], the performance of torque ripple reduction is further improved by utilizing predictive delay compensation to compensate for the inherent delay of current loop. In [10], a field-weakening method is proposed for the efficiency optimization of the system.

In the earlier literatures, DFIG is mainly investigated to integrate it into the dc power transmission system. However, the existence of slip rings and brushes degrades the performance of DFIG in reliability and longevity [11], while full-sized converter is usually required for a PMSG. As an alternative, brushless BDFIG, which eliminates the drawbacks caused by slip rings and brushes and inherits nearly all merits of DFIG, was rapidly developed recently [12], [13]. A typical BDFIG has two sets of stator windings. One is power winding (PW), while the other is control winding (CW), which is fed by a variable frequency and voltage power converter. Considering high reliability [14] and relative high torque density (1.73 N·m/kg) achieved in [15], BDFIG has increasingly become a promising candidate for offshore wind power generation, which has been illustrated by a conventional BDFIG-AC configuration [16], where torque ripple reduction under unbalanced grid is obtained through harmonic current injection at two times of fundamental frequency, and a dc microgrid application. Besides, since the frequency is no longer enslaved to ac grid, it becomes possible to decrease the synchronous speed and the gearbox ratio [17] and improve the low-voltage ride-through capability [18].

To impel potential application in dc grid, the operation of the BDFIG-DC system is expected to be discussed. Unlike ac-grid-connected conditions where the frequency and amplitude of the voltage is clamped by the ac mains and regulation of active and reactive powers are mainly focused on [19], the dc generation systems offer flexible regulation of the stator frequency independent of the rotor speed apart from active power regulation. It is worth noting that there does not physically exist reactive power interaction in a BDFIG-DC system due to its special structure. In addition, the diode bridge connected to a constant voltage dc grid applies a strong distorted voltage on the PW winding and injects current harmonics. The resulted interactions between PW flux linage and current harmonics produce a considerable torque ripple, which is the main cause of fatigue strength and wear of mechanical components and, therefore, ought to be suppressed.

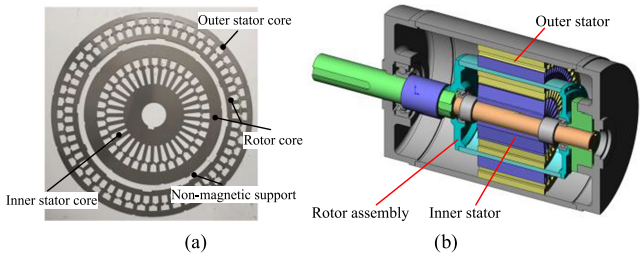

Fig. 1. DS-BDFIG. (a) Cross-sectional view. (b) Three-dimensional view.

Compared with existing literatures, the main contributions of this paper are as follows:

1) The theoretical analysis, along with the associated control strategy, of a novel BDFIG-DC system with a single PWM converter is presented for the first time.
2) A PW flux estimator is developed, on which the orientation angle is obtained and decoupled average torque and frequency controls are then realized.
3) Based on the investigation into torque ripple mechanism of the proposed configuration, the minimization of the torque ripple is obtained, even though the PW voltage/flux is highly distorted by the diode rectifier.
4) The feasibility and effectiveness of the BDFIG-DC system are sufficiently validated by simulations and experimental tests.

This paper is organized as follows. System configuration and modeling are illustrated in Section II. In Section III, the dynamic behaviors of the BDFIG-DC system are deduced. In Section IV, the control strategy of the BDFIG-DC system is provided, while Section V verifies the control strategy by simulation and experimental results.

II. System Configuration and Modeling

A. DS-BDFIG

The starting point is the description of the control object—a novel dual-stator BDFIG (DS-BDFIG), which can be conceptually conceived as the cascade of two wound rotor induction machines in radial direction [20]. With respect to this structure, the torque/power per volume as well as mechanical integrity proves to be improved over the traditional BDFIG by making full use of the internal vacancy [15]. As shown in Fig. 1, the DS-BDFIG consists of three parts: one outer stator with PW, an inner stator with CW, and a cup-shaped dual-layer wound rotor in between. From the perspective of control, the DS-BDFIG is almost exactly the same as other types of BDFIG, which indicates that the proposed system configuration and control strategies can also be applied to other BDFIGs.

B. Basic Configuration of the BDFIG-DC System

The configuration of the BDFIG-DC system based on a DS-BDFIG introduced is shown in Fig. 2, in which the PW

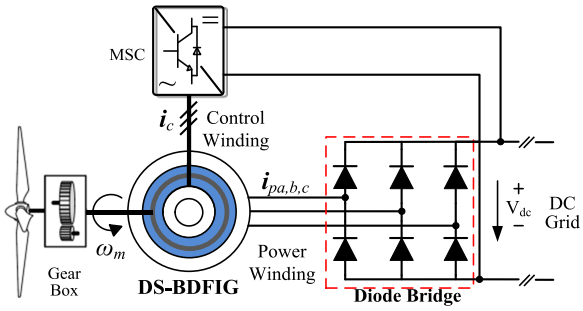

Fig. 2. Topology of the BDFIG-DC system based on DS-BDFIG.

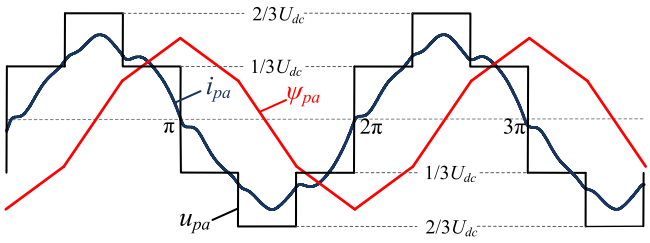

Fig. 3. Per-phase flux, voltage, and current waveforms of the BDFIG-DC system in CCM.

is connected to the dc link through diode bridge and GSC is therefore avoided, while the CW is fed by a machine-side converter (MSC). The MSC and PW are with a common dc link. Constant dc-link voltage is considered in this paper, which represents a strong dc grid. If the rectifier operates in mode 3/3 [7], which is also known as continuous conduction mode (CCM), the PW voltage is clamped to the three-step square wave, as shown in Fig. 3. In this figure, PW flux waveform and current are given as well.

As can be seen from Fig. 3, the PW flux linkage and current are not sinusoidal as a result of the distorted voltage

Acting as the core component of the energy conversion system, the DS-BDFIG is expected to operate in the doubly fed synchronous mode, in which ω_p and ω_c are the electrical angular frequencies of the PW and CW fields, respectively, $\omega_{rp} = \omega_p - p_p\omega_r$ and $\omega_{rc} = \omega_c - p_c\omega_r$ are the electrical angular frequencies of the rotor field induced by the outer stator and the inner stator, respectively. Thus, the synchronous condition is established if $\omega_{rp} = -\omega_{rc}$ and doubly fed synchronous operation is therefore achieved by the frequency constraint represented as

$$\omega_p + \omega_c = (p_p + p_c)\omega_r. \tag{1}$$

To provide an insight into the analysis of the DS-BDFIG, the equivalent circuit of the BDFIG is provided in Fig. 4. It is noteworthy that both electromagnetic quantities and machine parameters are constant by selecting the reference frames synchronous with PW and CW frequency, as shown in Fig. 5, where spatial relationships among the coordinates of $(\alpha\beta)p, (\alpha\beta)c, (dq)^1, (dq)^{5-}$, and $(dq)^{7+}$ are provided as well. Based on the equivalent circuit introduced, the dynamic of DS-BDFIG [21], which starts from the individual doubly fed induction generator (DFIG) model, is expressed in the dq reference frame rotating synchronously with the PW flux at the angular speed ω_p, denoted in the space vector notation as

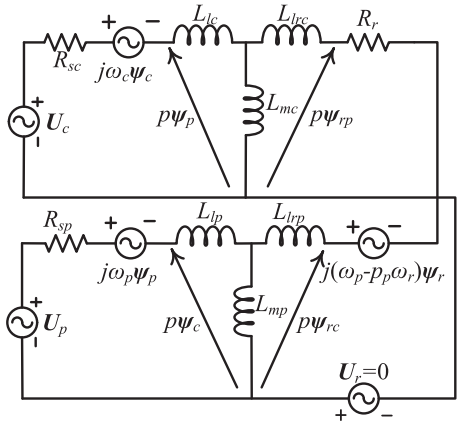

Fig. 4. Dynamic equivalent circuit of DS-BDFIG on the $d-q$ reference frame.

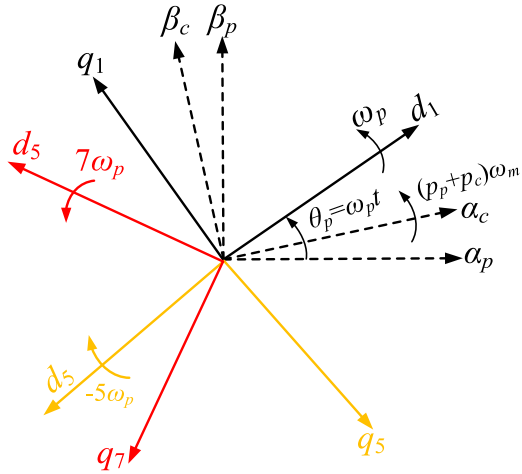

Fig. 5. Various reference frames in the genetic vector model.

$$\boldsymbol{u}_p = R_{sp}\boldsymbol{i}_p + j\omega_p\boldsymbol{\psi}_p + p\boldsymbol{\psi}_p \tag{2}$$

$$\boldsymbol{u}_r = R_r\boldsymbol{i}_r + j\omega_{rp}\boldsymbol{\psi}_r + p\boldsymbol{\psi}_r \tag{3}$$

$$\boldsymbol{u}_c = R_{sc}\boldsymbol{i}_c + j\omega_c\boldsymbol{\psi}_c + p\boldsymbol{\psi}_c \tag{4}$$

$$\boldsymbol{\psi}_p = L_p\boldsymbol{i}_p + L_{mp}\boldsymbol{i}_r \tag{5}$$

$$\boldsymbol{\psi}_r = L_r\boldsymbol{i}_r + L_{mp}\boldsymbol{i}_p - L_{mc}\boldsymbol{i}_c \tag{6}$$

$$\boldsymbol{\psi}_c = L_c\boldsymbol{i}_c - L_{mc}\boldsymbol{i}_r \tag{7}$$

where $\omega_{rp} = \omega_p - p_p\omega_r, \omega_c = \omega_p - (p_p + p_c)\omega_r, R_r = R_{rp} + R_{sp}$, and $L_r = L_{rp} + L_{sp}$.

III. Dynamic Behavior of the BDFIG-DC System

With respect to a BDFIG system, only CW current can be directly controlled with the assistance of voltage-source inverter. In order to achieve an effective regulation of the key physical parameters, such as electromagnetic torque and power, a step should be made to deduce such interrelations. As for a grid-connected BDFIG system, the relationship between PW current

and CW current should be deduced first. According to [22], the dynamics between CW and PW can be obtained.

By combining (2) and (3) and replacing $\boldsymbol{i}_r$, (3) becomes

$$0 = R_r \frac{\boldsymbol{\psi}_p - L_p \boldsymbol{i}_p}{L_{mp}} + j\omega_{rp}\left(L_r \frac{\boldsymbol{\psi}_p - L_p \boldsymbol{i}_p}{L_{mp}} + L_{mp}\boldsymbol{i}_p - L_{mc}\boldsymbol{i}_c\right). \tag{8}$$

And (8) can be rewritten as

$$\boldsymbol{i}_c = -\frac{\sigma_p L_r L_p}{L_{mc} L_{mp}}\boldsymbol{i}_p + \frac{L_r}{L_{mp} L_{mc}}\boldsymbol{\psi}_p \underbrace{- j\frac{R_r(\boldsymbol{\psi}_p - L_p \boldsymbol{i}_p)}{\omega_{rp} L_{mp} L_{mc}}}_{R_r \text{ related term}} \tag{9}$$

where $\sigma_p = 1 - L_{mp}^2/L_p L_r$, which is commonly defined as the leakage constant of PW. The first term in (9) corresponds to a linear relationship between two stator windings while the effect from the third term is governed by the value of rotor resistance R_r. This characteristic arises from the indirect coupling between PW and CW via the rotor. However, it is interesting that, as for a typical BDFIG, R_r is usually relatively small and can therefore be disregarded under some certain conditions considering the denominator of (9) is much larger.

As shown in Fig. 5, for the fundamental synchronous $(dq)^1$ reference frame, the d^1-axis rotates at the angular speed of ω_p. While for the $(dq)^5$ and $(dq)^7$ reference frames their d^5- and d^7-axes rotate at the angular speeds of $-5\omega_p$ and $7\omega_p$, respectively. It should be noted that the $\alpha\beta$ frame of CW rotates at the relative speed of $(p_p + p_c)\omega_m$, from the view of the PW stationary frame.

A. Deduction of Torque Ripple Equation

As a result of the diode commutation, the PW voltage is clamped to a three-step square wave and the corresponding flux linkage is expected to oscillate at six times of the PW fundamental frequency, as indicted earlier. Theoretically, torque ripple is expected to emerge when such voltage is imposed.

To give a direct intuition into the torque ripple, a complete torque ripple mechanism of a BDFIG-DC system can be explained by Fig. 6, where $\boldsymbol{i}$ and $\boldsymbol{\psi}$ are the current and flux vectors, respectively. The torque ripple mechanism is established on the principle that the flux vectors of different windings rotate in the same direction at the same speed will result in constant torque; otherwise, the torque will oscillate and vibrate. The frequency of harmonic quantities in CW and RW are deduced from the voltage imposed on PW, which have been previously presented in [23] and [24].

In Fig. 6, where generations of both average and harmonic torques of a BDFIG are illustrated, the block in the middle is the fundamental component; the block above is the fifth-harmonic component, while the block below is the seventh-harmonic component. When considering only fundamental and fifth- and seventh-order electrical variables, these exist 18 torque components in total among CW, PW, and rotor winding (RW) in a BDFIG-DC system. In Fig. 6, dashed lines indicate constant dc torques while solid and dashed-dotted lines indicate torque oscillating at the frequency $6\omega_p$ and $12\omega_p$, respectively. Strictly

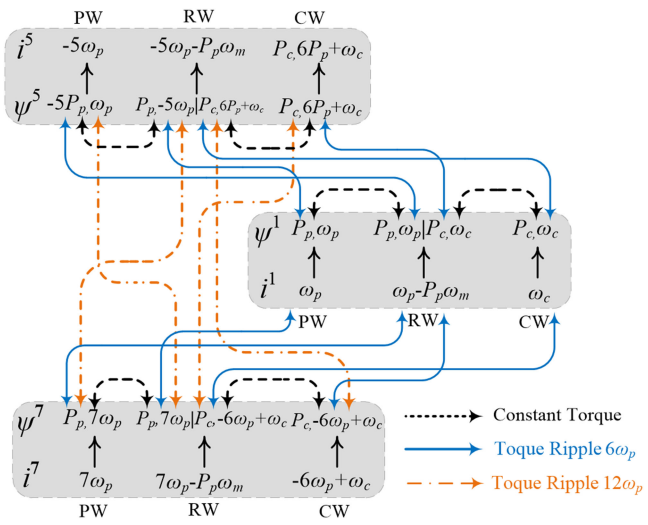

Fig. 6. Torque ripple mechanism of the BDFIG-DC system.

speaking, there exist two sources of 12th-harmonic torques, one from interaction between the fifth- and seventh-harmonic components while the other from the interaction among the fundamental, 11th-harmonic, and 13th-harmonic components, when considering both low order and high order.

In order to facilitate the torque analysis, some efforts need to be carried out to simplify the torque components derived in Fig. 6. Considering only the fundamental and low-order PW voltage, the PW voltage can be expressed as

$$\boldsymbol{u}_{pdq} = \boldsymbol{u}_{pdq}^1 + \boldsymbol{u}_{pdq}^5 e^{-j6\omega_p t} + \boldsymbol{u}_{pdq}^7 e^{j6\omega_p t}. \tag{10}$$

When replacing the PW voltage with flux linkage while ignoring the PW resistance, (11) can be further expressed as

$$\boldsymbol{\psi}_{pdq} = \frac{\boldsymbol{u}_{pdq}^1}{j\omega_p} - \frac{\boldsymbol{u}_{pdq}^5 e^{-j6\omega_p t}}{j5\omega_p} + \frac{\boldsymbol{u}_{pdq}^7}{j7\omega_p} e^{j6\omega_p t}. \tag{11}$$

From [16], the torque of a BDFIG is equal to

$$T_{em} = T_{emp} + T_{emc} = \frac{3p_p}{2} Im\{\hat{\psi}_p^+ i_p^+\} + \frac{3p_c}{2} Im\{\psi_c^+ \hat{i}_c^+\}. \tag{12}$$

Substituting ψ_c^+ with $\psi_p^+ L_{mc}/L_{mp} - i_p L_{mc} L_p/L_{mp} + L_c i_c$, the electromagnetic torque is given as

$$T_{em} = \frac{3p_p}{2} Im\{\hat{\psi}_p^+ i_p^+\} + \frac{3p_c}{2} Im \times \left\{\left(\frac{L_{mc}\psi_p^+}{L_{mp}} - \frac{L_{mc} L_p}{L_{mp}} i_p^+ + L_c i_c^+\right)\hat{i}_c^+\right\}. \tag{13}$$

By substituting (9) into (13) and ignoring R_r-related term, the BDFIG electromagnetic torque can be approximately

expressed as

$$\begin{aligned} T_{em} &= \frac{3p_p}{2} Im\{\hat{\psi}_p^+ i_p^+\} \\ &\quad + \frac{3p_c}{2} Im\left\{\left(\frac{L_{mc}\psi_p^+}{L_{mp}} - \frac{L_{mc}L_p i_p^+}{L_{mp}}\right)\right. \\ &\quad \left.\times\left(\frac{\sigma_p L_r L_p \hat{i}_p^+}{L_{mc}L_{mp}} - \frac{L_r\hat{\psi}_p^+}{L_{mp}L_{mc}}\right)\right\} \\ &= \frac{3p_p}{2} Im\{\hat{\psi}_p^+ i_p^+\} + \frac{3p_c}{2} Im \\ &\quad \times\left\{-\hat{\psi}_p i_p^+ \frac{L_r L_p - {L_{mp}}^2}{{L_{mp}}^2} + \hat{\psi}_p i_p^+ \frac{L_p L_r}{{L_{mp}}^2}\right\} \\ &= \frac{3(p_p + p_c)}{2} Im\{\hat{\psi}_p^+ i_p^+\}. \end{aligned} \tag{14}$$

Decomposing (14) into average torque and harmonic components yields

$$\begin{aligned} T_{em} &= T_{emdc} + T_{em\cos 6}\cos(6\omega_p t) + T_{em\sin 6}\sin(6\omega_p t) \\ &\quad + T_{em\cos 12}\cos(12\omega_p t) + T_{em\sin 12}\sin(12\omega_p t) \end{aligned} \tag{15}$$

where the subscripts dc, $\sin 6/\cos 6$, and $\sin 12/\cos 12$ represent the average component and the cosine/sine components with the frequencies of $6\omega_p$ and $12\omega_p$, respectively. The most significant component of the torque ripple is the sixth harmonic $T_{em\sin 6}$ and $T_{em\cos 6}$, which is given by (16) shown at the bottom of this page.

As represented in (16) the instantaneous electromagnetic torque produced by the BDFIG contains five components. Meanwhile, the average torque can be deduced as follows:

$$\begin{aligned} T_{emdc} &= \frac{3(p_p + p_c)}{2\omega_p} \\ &\quad \times\begin{bmatrix} -u_{pd1}^1 & -u_{pq1}^1 & \frac{u_{pd5}^5}{5} & \frac{u_{pq5}^5}{5} & -\frac{u_{pd7}^7}{7} & -\frac{u_{pq7}^7}{7}\end{bmatrix} \\ &\quad \times\begin{bmatrix} i_{pd1}^1 & i_{pq1}^1 & i_{pd5}^5 & i_{pq5}^5 & i_{pd7}^7 & i_{pq7}^7\end{bmatrix}^{-1}. \end{aligned} \tag{17}$$

B. Effect of Rotor Resistance on the Electromagnetic Torque Prediction

According to the torque estimation carried out in Section III-A using PW stator flux and current components, the BDFIG system is somehow simplified to a DFIG system when electromagnetic torque calculation is conducted, which is based on the assumption that the rotor resistance is near to zero and rotor speed of the BDFIG is far from the PW synchronous speed (ω_p/P_p). However, accuracy of electromagnetic torque predication is degraded and the effect of rotor resistance on electromagnetic torque should therefore be analyzed and evaluated.

From (9) and (13), the complete expression of electromagnetic torque can be given by

$$T_{em} = \frac{3(p_p + p_c)}{2} Im\{\hat{\psi}_p^+ i_p^+\} + T_{emR} \tag{18}$$

where

$$T_{emR} = \frac{3p_c}{2} Im\left\{j\frac{R_r(\psi_p^+ - L_p i_p^+)(\hat{\psi}_p^+ - L_p\hat{i}_p^+)}{{L_{mp}}^2\omega_{rp}}\right\}.$$

T_{emR} is defined as the torque component related to rotor resistance R_r. And this term can be further expressed as

$$\begin{aligned} T_{emR} &= \frac{3p_c R_r}{2} Im \\ &\quad \times\left\{j\frac{\left|\psi_p^+\right|^2 - L_p(i_p^+\hat{\psi}_p^+ + \hat{i}_p^+\psi_p^+) + {L_p}^2\left|i_p^+\right|^2}{\omega_{rp}{L_{mp}}^2}\right\}. \end{aligned} \tag{19}$$

Furthermore, the influence of T_{emR} on T_{em} is given as

$$\begin{aligned} D_T &= \frac{T_{emR}}{T_{em}} \\ &= \frac{p_c R_r Re\{\left|\psi_p^+\right|^2 - L_p(i_p^+\hat{\psi}_p^+ + \hat{i}_p^+\psi_p^+) + {L_p}^2\left|i_p^+\right|^2\}}{(p_p + p_c)\omega_{rp}{L_{mp}}^2 Im\{\hat{\psi}_p^+ i_p^+\}} \end{aligned} \tag{20}$$

where D_T is defined as the factor which describe the influence from T_{emR}. With respect to a BDFIG-DC system, a unity power factor is achieved. Thus, PW voltage and current are nearly aligned, which indicates that PW flux linkage is perpendicular to PW current since the phase displacement between the fundamental component of PW voltage and the PW current is small across the diode rectifier [8]. Then, (20) can be simplified to

$$D_T = \frac{R_r p_c\{\left|\psi_p^+\right|^2 + \left|i_p^+\right|^2 {L_p}^2\}}{(p_p + p_c)\omega_{rp}{L_{mp}}^2\left|\psi_p^+\right|\left|i_p^+\right|}. \tag{21}$$

It is noteworthy that D_T significantly rises when rotor speed increases. When rotor speed approaches PW synchronous speed (1000 r/min in this case), D_T becomes dramatically large. However, it is interesting to notice that the BDFIG is not targeted for wide-speed-range applications given in [25] and [26]. Under generating operating, the BDFIG usually works around $\pm 30\%$ of natural synchronous speed and rotor speed is kept away from PW synchronous speed.

$$\begin{aligned} \begin{bmatrix} T_{em\cos 6}^6 \\ T_{em\sin 6}^6\end{bmatrix} &= \frac{3(p_p + p_c)}{2\omega_p}\cdot\begin{bmatrix} -\frac{u_{pd5}^5}{5} + \frac{u_{pd7}^7}{7} & -\frac{u_{pq5}^5}{5} + \frac{u_{pq7}^7}{7} & u_{pd1}^1 & u_{pq1}^1 & u_{pd1}^1 & u_{pq1}^1 \\ -\frac{u_{pq5}^5}{5} - \frac{u_{pq7}^7}{7} & \frac{u_{pd5}^5}{5} + \frac{u_{pd7}^7}{7} & -u_{pq1}^1 & u_{pd1}^1 & u_{pq1}^1 & -u_{pd1}^1\end{bmatrix} \\ &\quad \times\begin{bmatrix} i_{pd1}^1 & i_{pq1}^1 & i_{pd5}^5 & i_{pq5}^5 & i_{pd7}^7 & i_{pq7}^7\end{bmatrix}^{-1} \end{aligned} \tag{16}$$

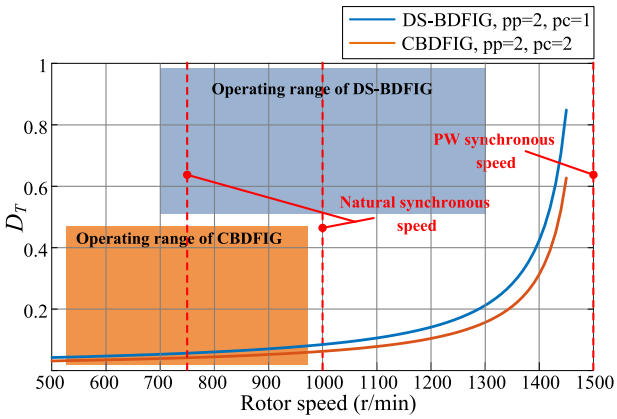

Fig. 7. Effect of rotor resistance on electromagnetic.

According to Fig. 7, where D_T is plotted with the parameters of three different kinds of BDFIG: DS-BDFIG discussed in this paper and Cascaded-BDFIG (CBDFIG) presented in [27], D_T is less than 0.25 for DS-BDFIG and less than 0.08 for CBDIG through their corresponding generation operating ranges. This feature makes T_{em} an acceptable approximation to the actual electromagnetic torque of BDFIG.

IV. Control Strategy of the BDFIG-DC System

When compared to AC grid-connected system, the most significant characteristic of this topology is the direct connection to dc grid through uncontrolled diode bridge, which makes the system control quite different from traditional BDFIG system. In general, two basic control targets are established for the generation system. One is PW frequency, which is established on the constraint PW frequency × PW flux ≈ constant; the other is average torque produced by the generator. Besides, being born with pulsating torque six times as high as of the fundamental frequency, the torque ripple is added as control target apart from frequency and average torque regulation.

A. PW Flux Orientation Angle Estimator

In a BDFIG-DC system, it becomes necessary to estimate the PW frequency since it is set as a control variable. In this paper, a PW frequency estimation approach is given. As reported in [9], the total harmonic distortion (THD) of the stator flux linkage is significantly smaller than that of the stator voltage. Thus, the PW flux linkage is more appropriate for frequency estimation. Due to the fact that inductance parameters, especially the self-inductance of CW [27], are normally influenced by saturation effect in a BDFIG, the PW voltage model is utilized for flux estimation instead of current model. Therefore, the PW flux linkage in dq frame can be given as

$$\psi_{pd} = \int (u_{pd} - R_{sp} \cdot i_{pd}) dt \tag{22}$$

$$\psi_{pq} = \int (u_{pq} - R_{sp} \cdot i_{pq}) dt. \tag{23}$$

Then, as shown in Fig. 8, the q-axis PW flux linkage ψ_{pq} is used as the error between the actual PW flux linkage angle

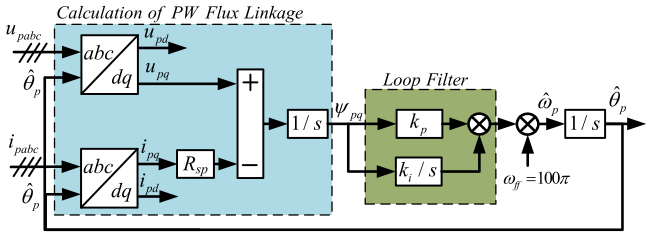

Fig. 8. Block diagram of orientation angle estimator.

and the estimated one. When the angle error ψ_{pq} is driven to be zero by PI controller, the estimated angle is the PW flux linage angle while the estimated frequency $\hat{\omega}_p$ is the PW frequency. In addition, the PI regulator also works as a loop filter for the estimator to filter out harmonics caused by the diode communication topology. Considering that the PW frequency is unlikely to undergo a sudden change, bandwidth of the PLL is set at 120 Hz, which is relatively low with respect to the main frequency component of ripple.

At the steady state, the q-axis PW flux linkage is driven to zero and PW flux linkage is aligned with the d-axis. Therefore, the CW d-axis current i_{cd}, whose reference value is obtained from the outer frequency loop, can be used to regulate the PW frequency.

B. Regulation of PW Frequency

Under steady-state, the BDFIG operates with almost constant EMF amplitude, which is determined by the voltage of dc link, and it can be considered that the PW flux linkage $\boldsymbol{\psi}_p$ is constant as well. Therefore, (2) can be simplified as

$$\boldsymbol{u}_p = R_{sp}\boldsymbol{i}_p + j\omega_p\boldsymbol{\psi}_p. \tag{24}$$

Splitting (24) into $d-q$ components gives

$$u_{pd} = R_{sp}i_{pd} - \omega_p\psi_{pq} \tag{25}$$

$$u_{pq}w = R_{sp}i_{pq} + \omega_p\psi_{pd}. \tag{26}$$

Considering that the PW flux linkage is aligned with the d-axis and substituting (5) and (6) into (26), ω_p can be expressed as

$$\omega_p = \frac{u_{pq} - R_{sp}i_{pq}}{L_{mp}L_{mc}/L_r i_{cd} + L_p\sigma_p i_{pd}}. \tag{27}$$

Due to the aforementioned assumption and simplification, $i_{pd} \approx 0$ at the steady state. By linearizing (27) around an equilibrium operating point, (27) can be approximated by its first-order Taylor expansion as

$$\Delta\omega_p = \frac{\Delta u_{pq}}{\psi_{pdE}} - \frac{R_{sp}}{\psi_{pdE}}\Delta i_{pq} - \frac{(u_{pqE} - R_{sp}i_{pqE})L_{mp}L_{mc}}{{\psi_{pdE}}^2 L_r}\Delta i_{cd} \tag{28}$$

where subscript E represents the equilibrium status. The disturbance Δu_{pq} includes minor effect from dc-link voltage variation, while Δi_{pq} indicates effect caused by voltage drop on PW resistance.

The small-signal model derived from (24) to (28) is represented in the block diagram of Fig. 9, which includes the

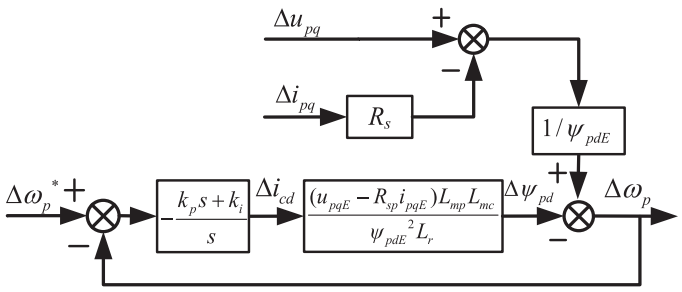

Fig. 9. Small-signal control loop of the PW frequency.

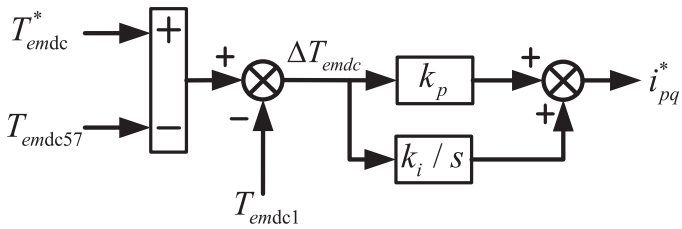

Fig. 10. Block diagram of average torque regulation.

frequency of the proportional–integral (PI) controller. For a small variation in the control variable Δi_{cd}, $\frac{(u_{pqE}-R_{sp}i_{pqE})L_{mp}L_{mc}}{\psi_{pdE}{}^2 L_r}$ represents a linearized open-loop transfer function from Δi_{cd} to $\Delta\omega_p$. Therefore, a PI controller can be used to control the frequency of PW, as shown in Fig. 9.

C. Regulation of Average Torque

According to the analysis of torque components in Section IV-A, the average torque is produced by flux vectors rotating in the same direction at the same speed, including the interaction between the fundamental component and the interaction among the harmonic components, which are denoted as T_{emdc1} and T_{emdc57} as

$$\begin{aligned} T_{emdc} = T_{emdc1} + T_{emdc57} &= \frac{3(p_p+p_c)}{2\omega_p}\begin{bmatrix} -u^1_{pd1} & -u^1_{pq1}\end{bmatrix} \\ &\times \begin{bmatrix} i^1_{pd1} & i^1_{pq1}\end{bmatrix}^{-1} \\ &+ \frac{3(p_p+p_c)}{2\omega_p}\begin{bmatrix} \frac{u^5_{pd5}}{5} & \frac{u^5_{pq5}}{5} & -\frac{u^7_{pd7}}{7} & -\frac{u^7_{pq7}}{7}\end{bmatrix} \\ &\times \begin{bmatrix} i^5_{pd5} & i^5_{pq5} & i^7_{pd7} & i^7_{pq7}\end{bmatrix}^{-1}. \end{aligned} \tag{29}$$

Since only i^1_{pq1} is responsible for average torque regulation, T_{emdc57} is subtracted from the reference value to guarantee the accuracy of average torque control, as shown in Fig. 10.

D. Control Targets Under DC-Grid-Connected Conditions

Based on the analysis given earlier, the electromagnetic torque will oscillate, when a dc grid is applied, and torque ripple minimization is set as the control target in this paper. According to (16), the magnitude of torque ripple is a function of PW currents in fundamental, fifth, and seventh sequences. Since i^1_{pd1} and i^1_{pq1} are responsible for frequency and average torque regulation, four degrees of freedom are spared for ripple reduction purpose. In this section, a simple and direct scheme is given, where i^5_{pd5} equals to i^5_{pq5} and i^7_{pd7} equals to i^7_{pq7}. Let $T^6_{em\sin 6} = T^6_{em\cos 6} = 0$, the reference PW current can be obtained by

$$\begin{cases} i^5_{pd5} = i^5_{pq5} = \left(\frac{u^5_{pd5}}{10} - \frac{u^5_{pq5}}{10} - \frac{u^7_{pd7}}{14} - \frac{u^7_{pq7}}{14}\right)\frac{i^1_{pd1}}{u^1_{pq1}} \\ \qquad + \left(\frac{u^5_{pd5}}{10} + \frac{u^5_{pq5}}{10} + \frac{u^7_{pd7}}{14} - \frac{u^7_{pq7}}{14}\right)\frac{i^1_{pq1}}{u^1_{pq1}} \\ i^7_{pd7} = i^7_{pq7} = \left(\frac{u^5_{pd5}}{10} + \frac{u^5_{pq5}}{10} - \frac{u^7_{pd7}}{14} + \frac{u^7_{pq7}}{14}\right)\frac{i^1_{pd1}}{u^1_{pq1}} \\ \qquad - \left(\frac{u^5_{pd5}}{10} - \frac{u^5_{pq5}}{10} + \frac{u^7_{pd7}}{14} + \frac{u^7_{pq7}}{14}\right)\frac{i^1_{pq1}}{u^1_{pq1}}. \end{cases} \tag{30}$$

After the PW harmonic sequence reference current is obtained, one further step should be conducted to derive the CW current reference. Similar to the procedure given in (8) and (9), the relationship between the harmonic sequences of PW and CW current can be deduced as (31) and (32)

$$\begin{aligned} \boldsymbol{i}^5_{c5} &= -\frac{\sigma_p L_r L_p}{L_{mc}L_{mp}}\boldsymbol{i}^5_{p5} + \frac{L_r}{L_{mp}L_{mc}}\boldsymbol{\psi}^5_{p5} \\ &+ j\frac{R_r(\boldsymbol{\psi}^5_{p5} - L_p\boldsymbol{i}^5_{p5})}{(5\omega_p + p_p\omega_r)L_{mp}L_{mc}} \end{aligned} \tag{31}$$

$$\begin{aligned} \boldsymbol{i}^7_{c7} &= -\frac{\sigma_p L_r L_p}{L_{mc}L_{mp}}\boldsymbol{i}^7_{p7} + \frac{L_r}{L_{mp}L_{mc}}\boldsymbol{\psi}^7_{p7} \\ &- j\frac{R_r(\boldsymbol{\psi}^7_{p7} - L_p\boldsymbol{i}^7_{p7})}{(7\omega_p - p_p\omega_r)L_{mp}L_{mc}}. \end{aligned} \tag{32}$$

As can be observed from the aforementioned two equations, effects from R_r become even slighter when compared with their counterparts in (9), since the denominators increase with a larger RW angular frequency. As a consequence, the harmonic sequence reference current $\boldsymbol{i}^{5*}_{c5}$ and $\boldsymbol{i}^{7*}_{c7}$ could be acquired after ignoring the coupling term caused by rotor resistance.

E. Design of the CW Current Loop

Once the CW current references are obtained by torque loop, frequency loop, and (30), the effective current controller should be designed to achieve an accurate control performance. When the current references are transformed to the fundamental synchronous frame, as shown in Fig. 11, where the block diagram of the whole BDFIG-DC control system is illustrated, ac components oscillating at $6\omega_p$ are expected to emerge. However, it is well known that the PI controller is not adequate to track the alternating reference signals. Thus, additional resonant (R) controllers tuned at $6\omega_p$, which have been widely discussed, are used for the CW current loop.

The transfer function of the PI-resonant (PIR) controller can be expressed as

$$G_{\mathrm{PI-R}} = K_{p-ic} + \frac{K_{i-ic}}{s} + \frac{2K_{r-ic}\omega_c s}{s^2 + 2\omega_c s + (6\omega_p)^2} \tag{33}$$

where K_{p-ic} and K_{i-c} are the gains of P and I controllers; ω_c denotes the cut-off frequency, which is used to take account of

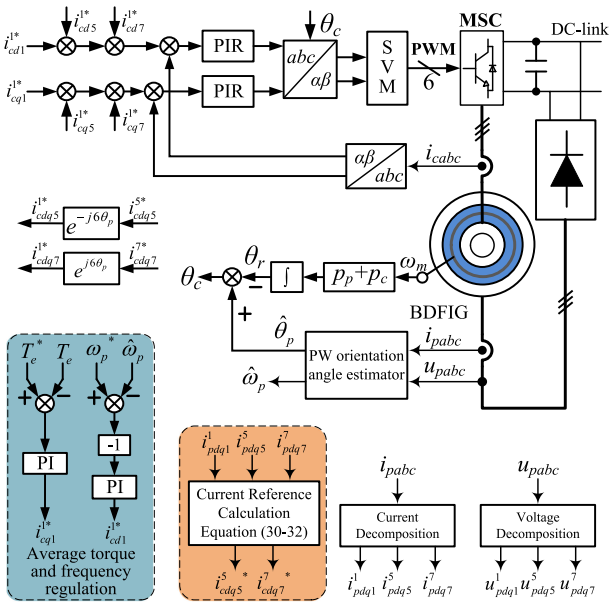

Fig. 11. Schematic diagram of the proposed control strategy for the BDFIG-DC system.

the PW frequency inaccuracy; K_{r-ic} is the gain of R controller; and ω_p is the angular speed of fundamental component of PW voltage.

Moreover, the CW current controllers can be depicted from (3), (4), and (9) as

$$\begin{aligned}\boldsymbol{u}_c^1 &= \left\{R_{sc}+\left(L_c-\frac{{L_{mc}}^2}{L_r\sigma_p}\right)p\right\}\boldsymbol{i}_c^1+j\omega_c\left(L_c-\frac{{L_{mc}}^2}{L_r\sigma_p}\right)\boldsymbol{i}_c^1 \\ &\quad+(p+j\omega_c)\frac{L_{cr}L_{pr}}{L_rL_p\sigma_p}\boldsymbol{\psi}_p^1 \\ &= R_{sc}\boldsymbol{i}_c^1+\left(L_c-\frac{{L_{mc}}^2}{L_r\sigma_p}\right)p\boldsymbol{i}_c^1+\boldsymbol{E}_c^1 \end{aligned} \tag{34}$$

where $\boldsymbol{E}_c^1$ denotes the equivalent back-EMF, which incorporates both cross-coupling terms and disturbance from the PW flux linkage to the CW current loop. Finally, the CW voltage reference can be expressed as

$$\boldsymbol{u}_{cdq}^{1*}=\boldsymbol{u}_{cdq}^{PI}+\boldsymbol{u}_{cdq}^{R}+j\omega_c\left(L_c-\frac{{L_{mc}}^2}{L_r\sigma_p}\right)\boldsymbol{i}_{cdq}^1 \tag{35}$$

where $\boldsymbol{u}_{cdq}^{PI}$ is the output of the PI controller, $\boldsymbol{u}_{cdq}^{R}$ is the output of the resonant compensator, and $j(L_c-\frac{{L_{mc}}^2}{L_r\sigma_p})\boldsymbol{i}_{cdq}^1$ is the cross-coupling term as a feed-forward item. The simplified inner loop system is shown in Fig. 12, where the control plant is simplified as a first-order system.

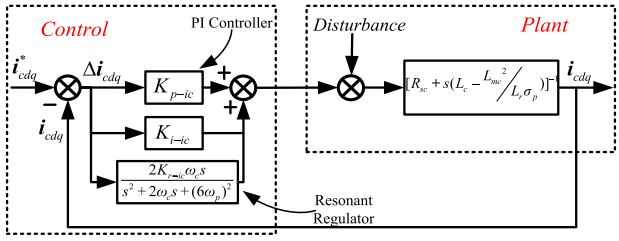

Fig. 12. Structure of the CW current loop.

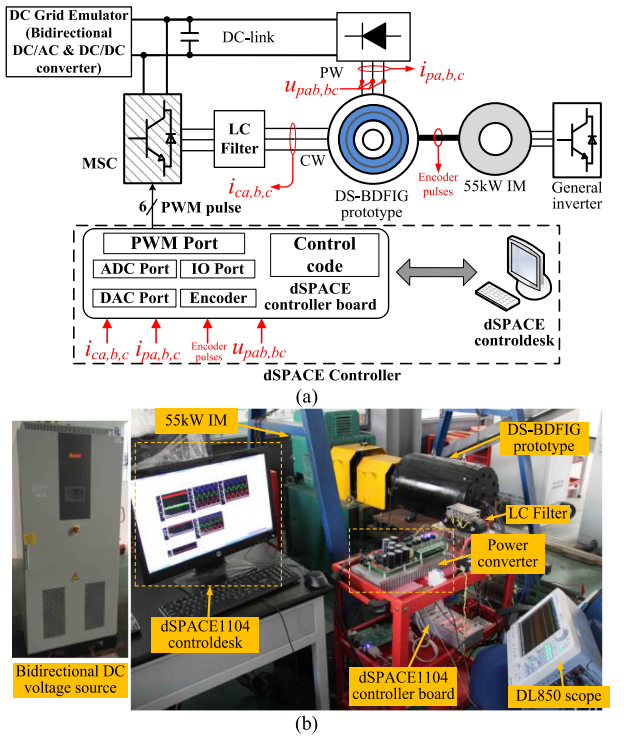

Fig. 13. Experimental test rig of the BDFIG-DC system. (a) Schematic diagram. (b) Photograph.

TABLE I
SPECIFICATION OF THE DS-BDFIG SYSTEM

Parameter	Value
Pole pair number p_p, p_c	2, 1
Natural-synchronous speed (r/min)	1000
Speed range (r/min)	700~1300
Winding resistance R_p, R_c (Ω)	1.3, 0.66
Leakage inductance L_{lp} L_{lc} (mH)	8.9, 18.1
Main self-inductance L_{mp}, L_{mc} (mH)	383, 647
Rotor winding resistance R_r (Ω)	2.263
Rotor winding inductance L_r (mH)	1057
Rated power (kW)	10
DC voltage (V)	100
Operating frequency (Hz)	50

V. SIMULATION AND EXPERIMENTAL RESULTS AND DISCUSSION

A. Experimental Configuration

In this section, the experimental verifications are conducted on the test rig shown in Fig. 13 to validate the proposed approach. As indicated before, a 10-kW DS-BDFIG prototype with an operation range from 750 to 1250 r/min, whose specifications are listed in Table I, is employed to test the proposed system configuration and control strategy. The DS-BDFIG is mechanically coupled to an induction machine, which is driven by a general inverter. The voltage and the current of CW and PW are measured directly through LEM LA 25 and LEM LV

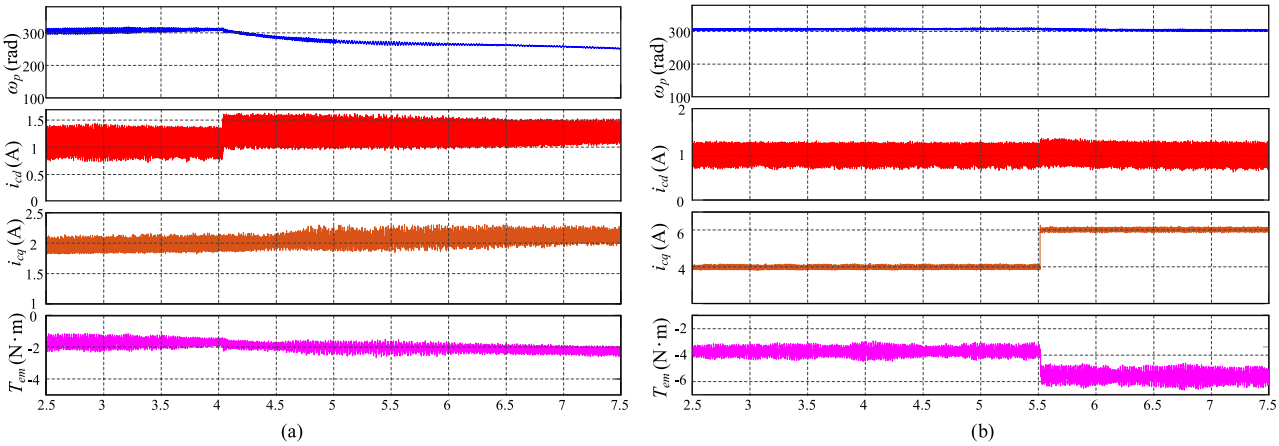

Fig. 14. Simulation waveforms of the CW current, the electromagnetic torque, and the PW frequency at asubsynchronous speed (650 r/min). (a) Responses to step in the d-axis CW current. (b) Responses to step in the q-axis CW current.

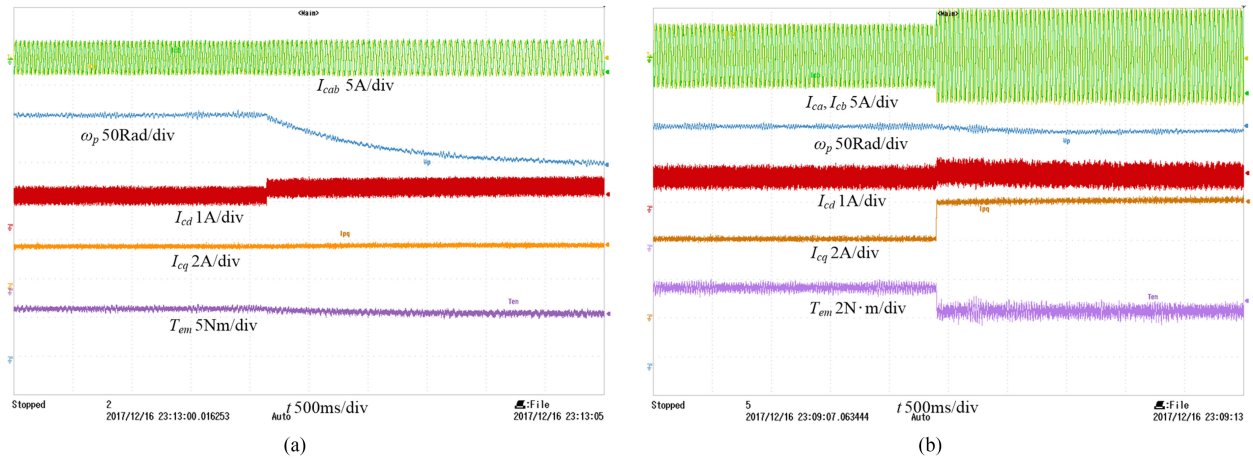

Fig. 15. Experimental waveforms of the CW current, the electromagnetic torque, and the PW frequency at a subsynchronous speed (650 r/min). (a) Responses to step in the d-axis CW current. (b) Responses to step in the q-axis CW current.

25 sensors. A bidirectional dc voltage source, which integrates a dc/ac converter and a dc/dc converter inside, is used to emulate the stable dc grid. In this case, the MSC is controlled by dSPACE1104 controller with a control frequency and switching rate as 5 and 20 kHz, respectively. The dc bus is kept at 100 V. All the waveforms are obtained by an eight-channel oscilloscope.

B. Open-Loop and Closed-Loop Results of the BDFIG-DC System

Simulations have been performed first with MATLAB/Simulink and parameters of the 10-kW DS-BDFIG prototype.

Fig. 14 shows the performance of the basic control system in open loop, which is used to demonstrate the decoupled control performance between the d-axis and the q-axis CW currents, where the frequency and the torque outer loop are disabled. Fig. 14(a) shows dynamic responses to a step change in the d-axis reference current i_{cq} at the instant $t = 4$ s, when the d-axis current reference is increased from 1.1 to 1.3 A. The results in Fig. 14(a) show the CW current i_{cd} and i_{cq}, the PW frequency $\hat{\omega}_p$, and the torque T_{em}. Clearly, when a d-axis current step occurs, the frequency drops, which corresponds to the small-signal analysis given in Section IV-B. Besides, the value of the electromagnetic torque is slightly influenced.

In Fig. 14(b), a step change on the q-axis CW current reference i_{cq} (from 2 to 4 A) is imposed at the instant $t = 5.5$ s, while the d-axis current is kept constant. As shown in Fig. 14(b), the electromagnetic torque rises drastically after the current step is imposed and, similarly to Fig. 14(a), the current change in i_{cq} has negligible impact on the PW frequency. These features make it possible to decouple the control of the PW frequency and electromagnetic torque.

In Fig. 15, the same test implemented in simulation verification is reported on the experimental rig.

To further understand the roles of CW the d-axis and q-axis current in frequency and torque regulation, Fig. 16 illustrates the closed-loop experimental results of the BDFIG-DC system. The major difference between Figs. 15 and 16 lies in whether outer frequency or outer torque ripple loop is enabled. In Fig. 16, the reference frequency is set to 50 Hz (100 π rad/s).

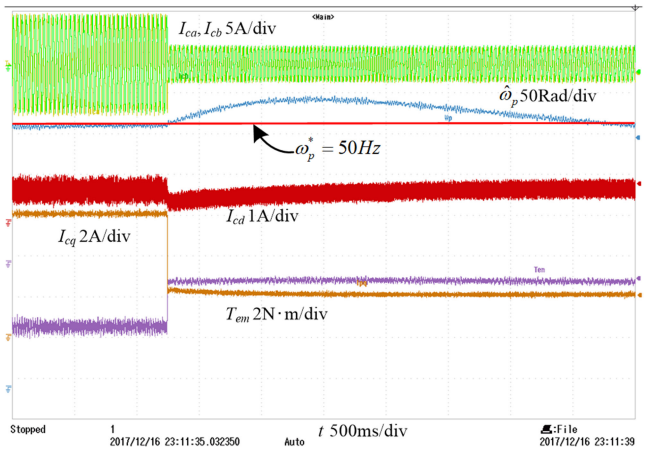

Fig. 16. Closed loop—CW phase currents, CW d- and q-axis currents, torque, and frequency waveforms and response.

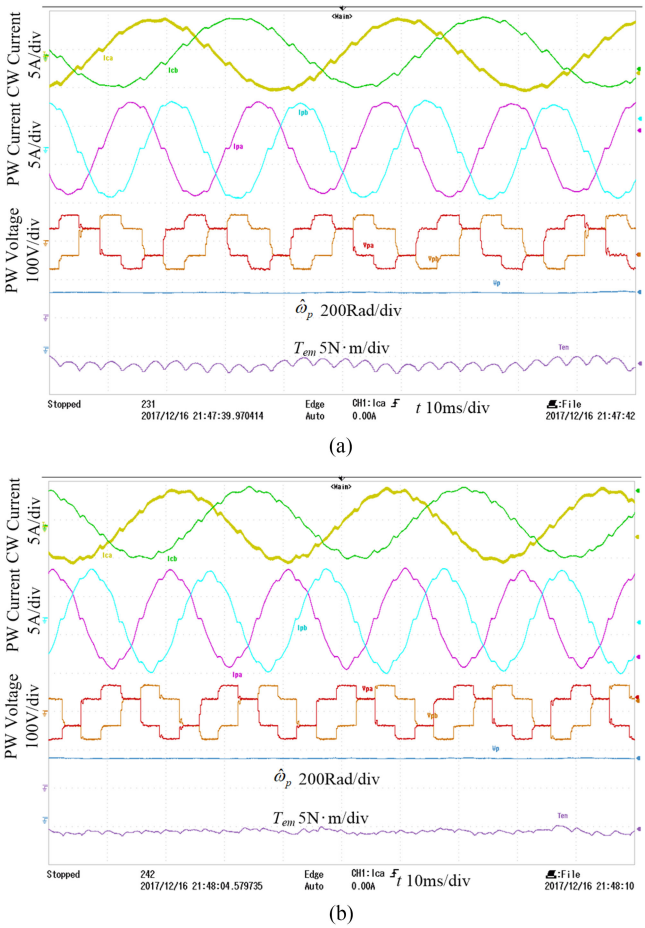

Fig. 17. Steady-state experimental results of the BDFIG-DC system with torque ripple reduction strategy. (a) Disabled. (b) Abled.

When the current step (from 6 to 2 A) is imposed on CW q-axis i_{cq}, the estimated PW frequency $\hat{\omega}_p$ is influenced. Nevertheless, the frequency outer loop is able to compensate such disturbance and annihilates the frequency error by adjusting the value of i_{cd}. As a consequence, the final frequency equals the reference value.

TABLE II
HARMONIC COMPONENTS IN PW VOLTAGE

Harmonic order	Content	Harmonic order	Content
5^{th}	17.2%	13^{th}	5.8%
7^{th}	11.1%	15^{th}	3.5%
11^{th}	7.1%	17^{th}	2.8%

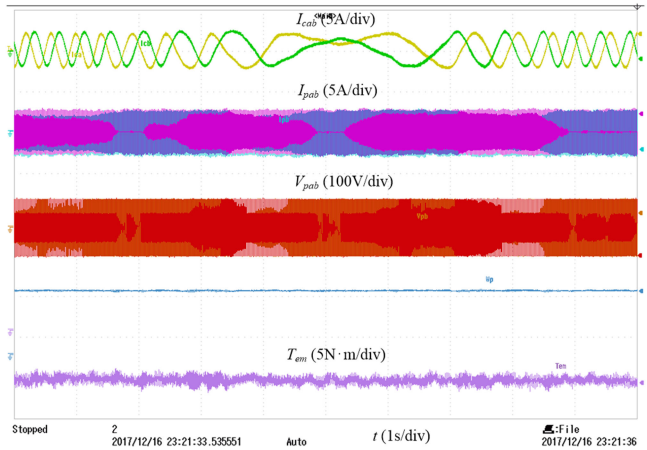

Fig. 18. Experimental results of the BDFIG-DC system during rotor speed variation from 950 to 1050 r/min.

C. Experimental Results with Torque Ripple Suppression Strategy Enabled

Fig. 17 shows the steady-state experimental results of the BDFIG-DC system before and after the torque ripple reduction strategy is activated. In the experimental test, the reference torque is set to −6 N·m. As can be seen from Table II, the harmonics of the PW voltage are mainly at 250 Hz (17.2%) and 350 Hz (11.1%). The torque ripple is about 0.6 N·m and its component is mainly at 300 Hz (9.2%), which corresponds to the theoretical analysis given in Section II. After the torque ripple strategy is enabled, only the torque ripple component at 600 Hz survives while the ripple component at 300 Hz drops below 0.08 N·m (around 1.4%), as shown in Fig. 17(b), and the residual ripple is due to the 12th harmonics. Furthermore, the PW frequency estimation is not influenced by the torque ripple reduction strategy.

D. Experimental Results With Rotor Speed Change

Fig. 18 shows the speed change of the BDFIG from the subsynchronous region (950 r/min) to the supersynchronous region (1050 r/min). Under this condition, the torque reference is set to −6 N·m. The CW current frequency varies from 2.5 to 0 Hz and then 2.5 Hz again. As the rotor speed changes, the average torque value stays constant at −6 N·m, which follows the torque reference quite well. Besides, the estimated PW frequency $\hat{\omega}_p$ is not influenced by the rotor speed variation in spite of some small fluctuations, which is acceptable. It can be seen that the proposed control strategy can also achieve stable operation regardless of the rotor speed variation.

VI. Conclusion

This paper presents a novel BDFIG-DC system with a single PWM converter to fully explore the potential of the BDFIG in dc microgrids and offshore wind power generation, where dc links are used and the system reliability is more emphasized. Contributions of this paper will lay a solid foundation for the practical application of the BDFIG in dc microgrids and thus are highlighted as follows:

1) A novel BDFIG-DC wind power conversion system is fully investigated. The uncontrolled diode bridge directly connected to the PW of the BDFIG eliminates the GSC, which benefits the system with lower cost and higher reliability.
2) The relationship between the CW fundamental current and the control targets, i.e., the average torque and PW frequency, is revealed. Based on the derived relationship, the PW frequency is found to be well controlled by the d-axis CW current, while the q-axis CW current can be used to control the average torque.
3) The torque ripple mechanism in the BDFIG-DC system is clarified and a harmonic torque cancellation strategy is then proposed, based on which a resonant current regulator is developed to suppress the inherent sixth torque ripple.
4) The superiority and effectiveness of the proposed system, along with the associated control strategy, are verified by simulation and experimental tests on a scaled-down DS-BDFIG prototype.

References

[1] E. M. D. Miguel, S. M. David, A. Santiago, and D. C. Edgardo, "Optimal operation of offshore wind farms with line-commutated HVDC link connection," *IEEE Trans. Energy Convers.*, vol. 25, no. 2, pp. 71–78, Jun. 2010.

[2] F. Nejabatkhah and Y. W. Li, "Overview of power management strategies of hybrid AC/DC microgrid," *IEEE Trans. Power Electron.*, vol. 30, no. 12, pp. 7072–7089, Dec. 2015.

[3] M. Cheng and Y. Zhu, "The state of the art of wind energy conversion systems and technologies: A review," *Energy Convers. Manage.*, vol. 88, pp. 332–347, Dec. 2014.

[4] M. F. Iacchetti, G. D. Marques, and R. Perini, "Operation and design issues of a DFIG stator-connected to a DC-net by a diode rectifier," *IET Electr. Power Appl.*, vol. 8, no. 8, pp. 310–319, Sep. 2014.

[5] G. D. Marques and M. F. Iacchetti, "Inner control method and frequency regulation of a DFIG connected to a DC link," *IEEE Trans. Energy Convers.*, vol. 29, no. 2, pp. 435–444, Jun. 2014.

[6] G. D. Marques and M. F. Iacchetti, "Stator frequency regulation in a field-oriented controlled DFIG connected to a dc link," *IEEE Trans. Ind. Electron.*, vol. 61, no. 11, pp. 5930–5939, Nov. 2014.

[7] M. F. Iacchetti, G. D. Marques, and R. Perini, "Torque ripple reduction in a DFIG-DC system by resonant current controllers," *IEEE Trans. Power Electron.*, vol. 30, no. 8, pp. 4244–4254, Aug. 2015.

[8] H. Nian, C. Wu, and P. Cheng, "Direct resonant control strategy for torque ripple mitigation of DFIG connected to DC Link through diode rectifier on Stator," *IEEE Trans. Power Electron.*, vol. 32, no. 9, pp. 6936–6945, Sep. 2017.

[9] G. D. Marques and M. F. Iacchetti, "Minimization of torque ripple in the DFIG-DC system via predictive delay compensation," *IEEE Trans. Ind. Electron.*, vol. 65, no. 1, pp. 103–113, Jan. 2018, doi: 10.1109/TIE.2017.2716860.

[10] G. D. Marques and M. F. Iacchetti, "Field-weakening control for efficiency optimization in a DFIG connected to a dc-link," *IEEE Trans. Ind. Electron.*, vol. 63, no. 6, pp. 3409–3419, Jun. 2016.

[11] H. Polinder, J. A. Ferreira, B. B. Jensen, A. B. Abrahamsen, K. Atallah, and R. A. McMahon, "Trends in wind turbine generator systems," *IEEE J. Emerg. Sel. Topics Power Electron.*, vol. 1, no. 3, pp. 174–185, Sep. 2013.

[12] M. Cheng, P. Han, G. Buja, and M. G. Jovanović, "Emerging multi-port electrical machines and systems: Past developments, current challenges and future prospects," *IEEE Trans. Ind. Electron.*, vol. 65, no. 7, pp. 5422–5435, Jul. 2018, doi: 10.1109/TIE.2017.2777388.

[13] P. Han, M. Cheng, S. Ademi, and M. G. Jovanovic, "Brushless doubly-fed machines: Opportunities and challenges," *Chin. J. Elect. Eng.*, vol. 4, no. 2, pp. 1–17, Jun. 2018.

[14] T. D. Strous, H. Polinder, and J. A. Ferreira, "Brushless doubly-fed induction machines for wind turbines: Developments and research challenges," *IET Electr. Power Appl.*, vol. 11, no. 6, pp. 991–1000, Jul. 2017.

[15] P. Han, M. Cheng, Y. Jiang, and Z. Chen, "Torque/power density optimization of a dual-stator brushless doubly-fed induction generator for wind power application," *IEEE Trans. Ind. Electron.*, vol. 64, no. 12, pp. 9864–9875, Dec. 2017.

[16] J. Chen, W. Zhang, B. Chen, and Y. Ma, "Improved vector control of brushless doubly fed induction generator under unbalanced grid conditions for offshore wind power generation," *IEEE Trans. Energy Convers.*, vol. 31, no. 1, pp. 293–302, Mar. 2016.

[17] S. Yan, A. Zhang, H. Zhang, J. Wang, and B. Cai, "An optimum design for DC-based DFIG system by regulating gearbox ratio," *IEEE Trans. Energy Convers* vol. 33, no. 1, pp. 223–231, Mar. 2018, doi: 10.1109/TEC.2017.2741104.

[18] M. F. Iacchetti, G. D. Marques, and R. Perini, "A scheme for the power control in a DFIG connected to a DC bus via a diode rectifier," *IEEE Trans. Power Electron.*, vol. 30, no. 3, pp. 1286–1296, Mar. 2015.

[19] S. Ademi and M. G. Jovanovic, "Vector control methods for brushless doubly fed reluctance machines," *IEEE Trans. Ind. Electron.*, vol. 62, no. 1, pp. 96–104, Jan. 2015.

[20] P. Han, M. Cheng, X. Wei, and Y. Jiang, "Steady-state characteristics of the dual-stator brushless doubly-fed induction generator," *IEEE Trans. Ind. Electron.*, vol. 65, no. 1, pp. 200–210, Jan. 2018.

[21] X. Wei, M. Cheng, W. Wang, P. Han, and R. Luo, "Direct voltage control of dual-stator brushless doubly fed induction generator for stand-alone wind energy conversion systems," *IEEE Trans. Magn.*, vol. 52, no. 7, pp. 1–4, Jul. 2016.

[22] S. Shao, E. Abdi, F. Barati, and R. McMahon, "Stator-flux-oriented vector control for brushless doubly fed induction generator," *IEEE Trans. Ind. Electron.*, vol. 56, no. 10, pp. 4220–4228, Oct. 2009.

[23] Y. Jiang, M. Cheng, and Q. Wang, "Control strategy for harmonic elimination in stand-alone dual-stator brushless doubly fed induction generators with nonlinear loads," in *Proc. 20th Int. Conf. Elect. Syst.*, Sydney, N.S.W., Australia, 2017, pp. 1–6.

[24] M. Cheng, Y. Jiang, P. Han, and Q. Wang, "Unbalanced and low-order harmonic voltage mitigation of stand-alone dual-stator brushless doubly fed induction wind generator," *IEEE Trans. Ind. Electron.*, vol. 65, no. 11, pp. 9135–9146, Nov. 2018, doi: 10.1109/TIE.2017.2779422.

[25] P. Han, M. Cheng, and Z. Chen, "Single-electrical-port control of cascaded doubly-fed induction machine for EV/HEV applications," *IEEE Trans. Power Electron.*, vol. 32, no. 9, pp. 7233–7243, Sep. 2017.

[26] P. Han, M. Cheng, and Z. Chen, "Dual-electrical-port control of cascaded doubly-fed induction machine for EV/HEV applications," *IEEE Trans. Ind. Appl.*, vol. 53, no. 2, pp. 1390–1398, Mar./Apr. 2017.

[27] J. Hu, J. Zhu, and D. G. Dorrell, "A new control method of cascaded brushless doubly fed induction generators using direct power control," *IEEE Trans. Energy Convers.*, vol. 29, no. 3, pp. 771–779, Sep. 2014.

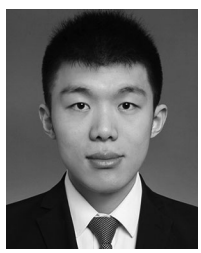

Yunlei Jiang (S'14) received the B.Sc. degree from Nanjing Normal University, Nanjing, China, in 2015, and the M.Sc. degree from the School of Electrical Engineering, Southeast University, Nanjing, in 2018. He is currently working toward the Ph.D. degree with the Department of Electrical and Computer Engineering, Wisconsin Electric Machines and Power Electronics Consortium (WEMPEC), University of Wisconsin-Madison.

His current research interests include the analysis and control of brushless ac machines in wind energy conversion systems and high-speed/high-power electrical drives.

Ming Cheng (M'01–SM'02–F'15) received the B.Sc. and M.Sc. degrees from Southeast University, Nanjing, China, in 1982 and 1987, respectively, and the Ph.D. degree from The University of Hong Kong, Hong Kong, in 2001, all in electrical engineering.

Since 1987, he has been with Southeast University, where he is currently a Chair Professor in the School of Electrical Engineering and the Director of the Research Center for Wind Power Generation. From January to April 2011, he was a Visiting Professor with the Wisconsin Electric Machine and Power Electronics Consortium, University of Wisconsin, Madison. His teaching and research interests include electrical machines, motor drives for electric vehicles, and renewable energy generation. He has authored or coauthored over 380 technical papers and 4 books and is the holder of over 100 patents in these areas.

Dr. Cheng is a Fellow of the Institution of Engineering and Technology. He was the Chair and Organizing Committee Member for many international conferences. He was a Distinguished Lecturer of the IEEE Industry Applications Society (IAS) in 2015/2016.

Peng Han (S'12–M'17) received the B.Sc. and Ph.D. degrees in electrical engineering from the School of Electrical Engineering, Southeast University, Nanjing, China, in 2012 and 2017, respectively.

From November 2014 to November 2015, he was a joint Ph.D. student funded by the China Scholarship Council with the Department of Energy Technology, Aalborg University, Aalborg, Denmark, where he was involved in the brushless doubly fed machines for wind energy conversion and high-power drives. He is currently a Research Scientist with the Department of Electrical and Computer Engineering, Center for High Performance Power Electronics (CHPPE), The Ohio State University, Columbus, OH, USA. His current research interests include electric machines and power electronics.

Qingsong Wang (S'14–M'17–SM'17) received the B.Sc. and M.Sc. degrees from Zhejiang University, Hangzhou, China, in 2004 and 2007, respectively, and the Ph.D. degree from the School of Electrical Engineering, Southeast University, Nanjing, China, in 2016.

From July 2004 to July 2005, he was an Engineer at Shihlin Electronic and Engineering Co., Ltd, Suzhou, China. From July 2007 to August 2011, he was an Engineer at the Global Development Center of Philips Lighting Electronics, Shanghai, China. In October 2010, he was promoted Senior Engineer. From August 2011 to September 2013, he was a Lecturer at PLA University of Science and Technology, Nanjing, China. Since 2017, he has been with the Southeast University, where he is currently a Lecturer in the School of Electrical Engineering. His current research interests include control and applications of power electronics to power systems, smart grids, and lighting drivers.

Xiaohu Wang received the B.Sc. and M.Sc. degrees in electrical engineering from the School of Electrical Engineering, Southeast University, Nanjing, China, in 2015 and 2018, respectively.

He is currently with Jiangsu Frontier Electric Technology Co., Ltd., Nanjing. His current research interests include design and control of high-performance induction motors.